Modulated magnetism and anomalous electronic transport in $Ce_3Cu_4As_4O_2$

Jiakui K. Wang,[1] Shan Wu,[2,*] Yiming Qiu,[3,4] Jose A. Rodriguez-Rivera,[3,4] Qingzhen Huang,[3] C. Broholm,[2,5] and E. Morosan[1,*]

[1]*Department of Physics and Astronomy, Rice University, Houston, Texas 77005, USA*
[2]*Department of Physics and Astronomy and Institute for Quantum Matter, Johns Hopkins University, Baltimore, Maryland 21218, USA*
[3]*NIST Center for Neutron Research, National Institute of Standards and Technology, Gaithersburg, Maryland 20899, USA*
[4]*Department of Materials Science, University of Maryland, College Park, Maryland 20742, USA*
[5]*Department of Materials Science and Engineering, Johns Hopkins University, Baltimore, Maryland 21218, USA*

(Received 11 April 2015; revised manuscript received 28 July 2016; published 29 August 2016)

The complex magnetism and transport properties of tetragonal $Ce_3Cu_4As_4O_2$ were examined through neutron scattering and physical property measurements on polycrystalline samples. The lamellar structure consists of alternating layers of $CeCu_4As_4$ with a single square Ce lattice and Ce_2O_2 bilayers. Peaks in the specific heat at the Néel temperature $T_N = 24$ K, $T_2 = 16$ K, and $T_3 = 1.9$ K indicate three magnetic phase transitions or distinct crossover phenomena. For $T < T_N$ neutron diffraction indicates the development of ferromagnetic ab sheets for both Ce sites, with alternating polarization along $\mathbf{c}$, and a wave vector $\mathbf{k}_1 = \mathbf{c}^*$. For $T < T_2$, quasi-two-dimensional low-energy spin fluctuations with $\mathbf{k}_2 = \frac{1}{2}\mathbf{a}^*$ and polarized perpendicular to $\mathbf{k}_2$ are suppressed. The data are consistent with quasi-two-dimensional antiferromagnetic order in the $CeCu_4As_4$ planes polarized along the $\mathbf{k}_2$ wave vector. T_3 marks a spin-flop transition where the $\mathbf{k}_1$ staggered magnetization switches to in-plane polarization. There are significant transport anomalies associated with the transitions, in particular a substantial reduction in resistivity for $T < T_N$. At $T = 100$ mK the magnetic correlation length exceeds 75 Å and the $\mathbf{k}_1$ modulated staggered moment is 0.85 μ_B, which matches the 0.8 μ_B saturation magnetization achieved for $\mu_0 H = 7$ T at $T = 2$ K. We trace the unusual sequence of magnetic transitions to competing interactions and anisotropies in the alternating quasi-two-dimensional magnetic layers.

DOI: 10.1103/PhysRevB.94.064430

I. INTRODUCTION

As spin degeneracy is lifted through crystal field and exchange interactions, intermetallic compounds containing rare-earth ions display intricate thermodynamic, magnetic, and transport anomalies. In the Kondo effect dilute rare-earth impurities in a metal give rise to a minimum in the resistivity due to resonant electron scattering from the impurity spin [1,2]. When the rare-earth ions form a full crystalline lattice and when hybridization with more dispersive bands is sufficiently strong, a full band gap can open in so-called Kondo insulators which may support topologically protected surface states [3–5]. The Kondo lattice regime between these limits is defined by an intricate balance between intersite superexchange and intrasite Kondo screening [6]. When the former interactions prevail, magnetic order occurs concomitant with transport anomalies, while the ground state in the latter case is a heavy Fermi liquid (FL). At the quantum critical point (QCP) where these phases meet, there are non-Fermi-liquid (NFL) characteristics and in some cases superconductivity [7,8].

The search for materials to expose this strongly correlated regime recently led to the discovery of a family of rare-earth-bearing quasi-two-dimensional metals of the form $R_3T_4As_4O_{2-\delta}$ [9–11] that is structurally related to the iron superconductors. Here R indicates a rare-earth ion and T a transition-metal ion. While T appears to be nonmagnetic in this structure [9], it strongly influences the sequence of transitions so that there are three transitions for $Ce_3Cu_4As_4O_2$ but just a single low-temperature transition for $Ce_3Ni_4As_4O_2$. The presence of *two* distinct rare-earth sites appears to underlie the complicated magnetic and transport properties of these materials. Focusing on $Ce_3Cu_4As_4O_2$, we seek in this paper to understand the physics underlying the previously reported sequence of phase transitions in this class of materials. While the absence of single-crystalline samples limits the specificity of our conclusions, the combination of thermodynamic, transport, and neutron scattering data that we shall report, as well as *ab initio* band structure calculations, provides an atomic-scale view of the intricate electronic properties of these materials. It is also apparent, however, that the complexity of the material is such that a full understanding will require much more detailed experiments that can only be carried out on single-crystalline samples.

So far our experiments indicate that incompatible in-plane magnetic interactions and magnetic anisotropies produce separate as well as coordinated magnetic phase transitions reminiscent of phase transitions in magnetic multilayer thin-film structures. The strongly anisotropic nature of the cerium spins and/or their interactions also plays an important role by allowing for a thermodynamic phase transition for an isolated 2D layer. The highest-temperature transition at $T_N = 24$ K is to an antiferromagnetic (AFM) stacking of ferromagnetically (FM) aligned tetragonal layers of spins oriented along the c axis, with characteristic magnetic wave vector $\mathbf{k}_1 = 1.0(2)\mathbf{c}^*$. This order is predominantly associated with the Ce_2O_2 layers. The $T_2 = 16$ K transition is associated with the *loss* of low-energy spin fluctuations in the square sublattice $CeCu_4As_4$. While we do not have direct diffraction evidence for this, the nature of the paramagnetic spin fluctuations that are suppressed and the fact that we do not detect additional diffraction for $T < T_2$ indicate the spin structure in $CeCu_4As_4$ layers for

*Corresponding authors: swu32@jhu.edu; emorosan@rice.edu

$T < T_2$ has a characteristic wave vector $\mathbf{k}_2 = 0.50(2)\mathbf{a}^*$ with spins oriented along $\mathbf{k}_2$. Such longitudinally striped structures are also found among iron spins in the parent compounds of iron superconductors [12,13]. The lowest-temperature transition at $T_3 = 1.9$ K is associated with the development of a component of the $\mathbf{k}_1$-type magnetic order polarized within the basal plane. Indeed the data are consistent with the rotation of the entire polarization of Ce_2O_2 layers into the basal plane and perpendicular to an anisotropic striped AFM of the $CeCu_4As_4$ layers. The paper thus exposes an intricate interplay between distinct forms of rare-earth magnetism in the two different layers that make up $Ce_3Cu_4As_4O_2$.

After the methods section, our experimental results and initial observations are presented in Sec. III followed by analysis in Sec. IV. Section V draws together a physical picture of $Ce_3Cu_4As_4O_2$ and in the concluding section, Sec. VI, we put the results into the broader context of the $R_3T_4As_4O_2$ family of compounds and rare-earth-based strongly correlated electron systems in general.

II. METHODS

A. Synthesis and bulk measurements

Polycrystalline $Ce_3Cu_4As_4O_2$ was synthesized using a previously described solid-state method [9]. The sample employed for neutron scattering was a loose powder with a total mass of 5.8 g.

Magnetization measurements for temperatures between 2 K and 300 K were performed in a Quantum Design (QD) magnetic property measurement system (MPMS) [14] in magnetic fields up to 7 T. Specific-heat measurements were performed in a QD physical property measurement system (PPMS) [14], using an adiabatic relaxation method for temperature down to 0.4 K and fields up to 9 T. The dc electrical resistivity was measured on dense samples in the QD PPMS [14], using a standard four-point-contact method.

B. Neutron scattering

All neutron scattering experiments were conducted on instrumentation at the NIST Center for Neutron Research. For determination of the chemical structure powder diffraction data was acquired on BT1 using the Ge(311) monochromator $\lambda = 1.5398$ Å, with 60-inch in-pile collimation and the standard 20-inch and 7-inch collimation before and after the sample, respectively. For this measurement the powder sample was held in a thin-walled vanadium can with ^{4}He as exchange gas and the sample was cooled by a closed-cycle system. Rietveld refinement of the BT1 data was carried out using the General Structure Analysis System (GSAS) [15].

To detect magnetic diffraction from the relatively small moment magnetism of $Ce_3Cu_4As_4O_2$, high-intensity diffraction data were acquired for temperatures between 50 mK and 45 K on the Multi-Axis Crystal Spectrometer (MACS) at NIST [16]. For these long-wavelength measurements the powder was held in a thin-walled aluminum can with ^{4}He as exchange gas. A total of three different MACS experiments employing as many cryogenic systems contributed to the paper: In May 2013 we used an "orange" ^{4}He flow cryostat with access to temperatures from 1.5 K to 50 K. In November 2013 we used an Oxford Instruments dilution fridge with an 11.5 T magnet for the temperature range from 0.05 K to 14 K. Finally in May 2014 a dilution insert with access to temperatures from 0.1 K to 40 K was employed.

The incident and final neutron energies on MACS were defined by PG(002) monochromatization to be 5 meV. The full double-focusing configuration of the MACS monochromator was used for temperature scans while higher-resolution data were collected with the monochromator set for vertical focusing only and the beamwidth limited to 10 cm at the pre-monochromator beam aperture. The horizontal angular divergence of the incident neutron beam was 3.8° and 0.6° for the doubly and singly focused configurations, respectively.

A second set of energy-integrating detectors on MACS were utilized in this experiment. These "two-axis" detectors are behind the PG(002) double-bounce analyzers and detect scattered neutrons without energy discrimination. With an incident energy $E_i = 5$ meV and a beryllium filter between the powder sample and the analyzer the measured quantity can be written as follows [17]:

$$\frac{d\sigma}{d\Omega} = r_0^2 \int_0^{E_i} \sqrt{1 - \frac{\hbar\omega}{E_i}} \left| \frac{g}{2} F(Q_\omega) \right|^2 2\tilde{\mathcal{S}}(Q_\omega,\omega)\hbar d\omega. \quad (1)$$

Here $Q_\omega = |\mathbf{k}_i - \mathbf{k}_f|$, $\mathbf{k}_i$ and $\mathbf{k}_f$ being the wave vectors of incident and scattered neutrons, respectively, and $\tilde{\mathcal{S}}(Q_\omega,\omega)$ is the spherically averaged dynamic correlation function defined so as to include elastic scattering.

For the ultimate sensitivity to weak temperature-dependent scattering we plot and analyze temperature difference intensity data from the spectroscopic detectors on MACS. While this removes T-independent scattering on average, thermal expansion produces peak derivative line shapes in place of nuclear Bragg peaks. These features can be accounted for quantitatively based on thermal expansion coefficients and a Rietveld refinement [18] of the nuclear diffraction data as follows.

Using angular variables as is customary for monochromatic beam diffraction data, the Rietveld refined nuclear diffraction pattern is written as follows:

$$\mathcal{I}(\theta) = \mathcal{C} \sum_\tau \frac{I(\tau)}{2\sigma(\tau)} g\left(\frac{\theta - \Theta(\tau)}{\sigma(\tau)}\right). \quad (2)$$

Here $\mathcal{C}$ is the ratio between the experimental count rate and the macroscopic scattering cross section of the sample, 2θ is the scattering angle, τ indicates distinct reciprocal lattice vectors, $2\sigma(\tau)$ is the standard deviation for 2θ near the Bragg peak at scattering angle $2\Theta(\tau)$, and $g(x) = \exp(-x^2/2)/\sqrt{2\pi}$ is a unity-normalized Gaussian distribution. $I(\tau)$ is the 2θ-integrated powder cross section for $|\vec{\tau}| = \tau$, which can be expressed as

$$I(\tau) = \frac{4\pi^2 \tan\Theta}{v_0 \tau^3} N \sum_{|\vec{\tau}|=\tau} |F(\vec{\tau})|^2. \quad (3)$$

Here v_0 is the unit cell volume, N is the number of unit cells in the sample, and $F(\vec{\tau})$ is the unit cell structure factor including Debye-Waller factors.

Thermal expansion gives rise to a small shift in the scattering angle that can be written as follows:

$$\Delta\Theta = \frac{\Delta\tau}{\tau}\tan\Theta. \tag{4}$$

Neglecting changes in the intensity of nuclear Bragg peaks, the resulting difference intensity is given by

$$\Delta\mathcal{I}(\theta) = \frac{\partial\mathcal{I}(\theta)}{\partial\Theta}\Delta\Theta \tag{5}$$

$$= \mathcal{C}\sum_{\tau}\frac{I(\tau)}{2\sigma(\tau)}g'\left(\frac{\theta-\Theta(\tau)}{\sigma(\tau)}\right) \times\left(-\frac{1}{\sigma(\tau)}\right)\frac{\Delta\tau}{\tau}\tan\Theta(\tau). \tag{6}$$

Here $g'(x) = -xg(x)$. In general we have

$$\frac{\Delta\tau}{\tau} = \sum_i \frac{\partial\ln\tau}{\partial a_i}\Delta a_i, \tag{7}$$

where the summation is over all temperature-dependent lattice parameters including angular variables. In the present case of persistent tetragonal symmetry we have

$$\frac{\Delta\tau}{\tau} = -\left[[1-(\hat{\tau}_\parallel)^2]\frac{\Delta a}{a} + (\hat{\tau}_\parallel)^2\frac{\Delta c}{c}\right], \tag{8}$$

where $\hat{\tau}_\parallel$ is the projection of the unit vector $\hat{\tau}$ on the tetragonal c axis. Having determined $\sigma(\tau)$ and $I(\tau)$ from Rietveld refinement in the paramagnetic phase, we then Rietveld-refined the difference between the low and high T data with a functional consisting of the magnetic diffraction profile plus Eq. (6) allowing only for adjustable thermal expansion coefficients $\Delta a/a$ and $\Delta c/c$ [Eq. (8)]. The magnetic diffraction profile was developed using representation analysis as implemented in SARAh [19] and FULLPROF [20].

C. Electronic structure

Band structure calculations were performed using the full-potential linearized augmented plane wave (FP-LAPW) method implemented in the WIEN2k package [21]. The Perdew, Burke, and Ernzerhof version of the generalized gradient approximation [22] (PBE-GGA) was used for the exchange correlation potential and an on-site Coulomb repulsion of 5 eV was added to Ce sites to approximately account for electronic correlations in the narrow $4f$ bands [23,24]. Because the Ce states do not contribute to the electronic states at the Fermi level, spin-orbit coupling was not included in the calculation. The lattice parameters and atomic positions used for the calculation were taken from the neutron diffraction refinement at $T = 300$ K and are listed in Table I.

III. EXPERIMENTAL RESULTS

A. Chemical structure

The low-temperature ($T = 5$ K) crystal structure was determined from the Rietveld refinement of the powder neutron diffraction data ($\chi^2 = 2.7$) shown in Fig. 1. A single phase fit can account for the data with space group $I4/mmm$. Powder x-ray diffraction data had indicated a small oxygen deficiency in most reported $R_3T_4As_4O_{2-\delta}$ compounds (T = Ni or Cu) [9]. However, the inset to Fig. 1 shows the refinement

TABLE I. $T = 300$ K atomic positions for $Ce_3Cu_4As_4O_2$ with space group $I4/mmm$ determined by the Rietveld analysis [15] of neutron powder diffraction data. The corresponding reduced χ^2 measure of goodness of fit is $\chi^2 = 2.7$. The room temperature lattice constants are $a = 4.077\,33(10)$ Å and $c = 27.4146(9)$ Å.

Atom	Site	x	y	z	U_{iso} (Å)
Ce_1	2a	0	0	0	0.0088(6)
Ce_2	4e	1/2	1/2	0.2069(1)	0.0088(6)
Cu	8g	1/2	0	0.0975(5)	0.0133(4)
As_1	4e	0	0	0.1459(1)	0.0067(4)
As_2	4e	1/2	1/2	0.0454(2)	0.0067(4)
O	4d	1/2	0	1/4	0.0051(5)

of the oxygen stoichiometry in $Ce_3Cu_4As_4O_{2-\delta}$ based on the present neutron data, which yields the best refinement (lowest χ^2) for $\delta = 0.00(5)$ and therefore indicates that the compound is stoichiometric. No magnetic diffraction is visible in the BT1 data. This is however not inconsistent with the MACS data where the strongest magnetic peak at $T = 5$ K has an integrated intensity of just 0.4% of the strongest nuclear peak. The magnetic peaks are too weak to be detected by BT1. A summary of the structural information is provided in Tables I and II.

Illustrated in Fig. 2(a), the structure of $Ce_3Cu_4As_4O_2$ consists of alternating layers of $CeCu_4As_4$ (blue box) and Ce_2O_2 (red box). In $CeCu_4As_4$, Ce atoms lie at the vertices of a simple square lattice sandwiched between Cu_2As_2 layers. This structural unit is found in the $ThCr_2Si_2$ structure, which is familiar from 122 iron superconductors such as $BaFe_2As_2$ where Ba occupies the site equivalent to Ce in the $CeCu_4As_4$ layer [12]. There are also a number of heavy-fermion systems with a magnetic ion on this site including CeT_2Si_2 [25–28], (T = Pd, Ru, Rh, Cu), and URu_2Si_2 [29].

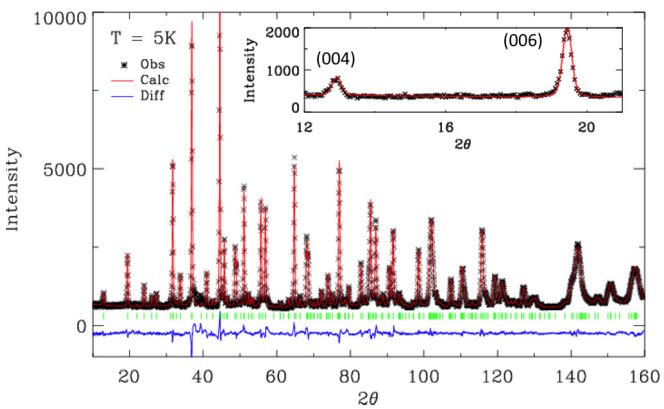

FIG. 1. Rietveld analysis of neutron diffraction from $Ce_3Cu_4As_4O_2$ powder at $T = 4.5$ K. The data were acquired on BT1 at NIST with $\lambda = 1.5398$ Å, with a Ge(311) monochromator and 60-inch in-pile collimation. The red line shows the GSAS fit [15]. The blue line shows the difference between model and diffraction data, while the green vertical lines show the calculated peak positions. The inset shows the detailed fit near the (004) and (006) nuclear Bragg peaks. All peaks are resolution limited and the Rietveld fit detailed in Table II provides an acceptable account of the data.

TABLE II. $T = 4.5$ K atomic positions for $Ce_3Cu_4As_4O_2$ in space group $I4/mmm$ determined by the Rietveld analysis [15] of powder diffraction data. The corresponding reduced χ^2 measure of goodness of fit is $\chi^2 = 3.4$. The corresponding lattice constants are $a = 4.063\,44(9)$ Å and $c = 27.3365(7)$ Å.

Atom	Site	x	y	z	U_{iso} (Å)
Ce_1	2a	0	0	0	0.0029(5)
Ce_2	4e	1/2	1/2	0.2068(1)	0.0029(5)
Cu	8g	1/2	0	0.0973(4)	0.0030(5)
As_1	4e	0	0	0.1462(7)	0.0002(3)
As_2	4e	1/2	1/2	0.04504(7)	0.0002(3)
O	4d	1/2	0	1/4	0.0007(4)

In the Ce_2O_2 layer, a 45° rotated square lattice of O with lattice parameter $a/\sqrt{2}$ is sandwiched by square lattices of Ce with lattice parameter a, such that half of the squares of the O lattice have Ce above and the other half have Ce below. This structural element is also found in the 1111-type Fe superconductors and specifically in CeFeAsO [30] and CeNiAsO [31,32].

B. Magnetic neutron scattering

1. Temperature dependence

Three peaks in the specific heat of polycrystalline $Ce_3Cu_4As_4O_2$ were previously reported and associated with magnetic transitions [9]. In order of decreasing temperature, we shall denote the corresponding phases by I ($T_2 < T < T_N$), II ($T_3 < T < T_2$), and III ($T < T_3$), respectively. In search for the associated atomic-scale magnetic correlations, we acquired neutron diffraction data for temperatures between 1.5 K ($<T_3$) and 40 K ($>T_N$) using a high-intensity configuration of the MACS spectrometer. For sensitivity to weak temperature-dependent scattering we subtract a high-statistics data set acquired at $T = 32$ K and plot the difference data as a color image in Fig. 3. The MACS instrument offers simultaneous energy-resolved data and final energy-integrated data shown respectively in Fig. 3(a) and Fig. 3(b). Coincident with each of the transition regimes inferred from specific-heat data [9]

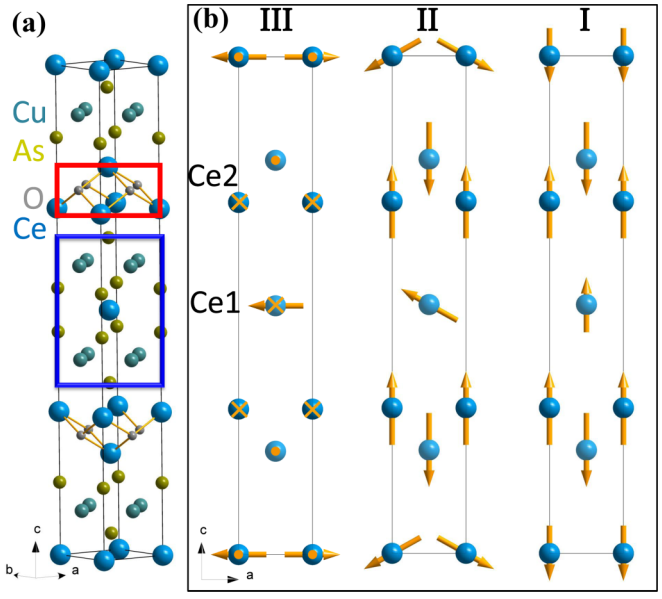

FIG. 2. (a) $Ce_3Cu_4As_4O_2$ crystal structure with space group $I4/mmm$. (b) Spin structures proposed for the magnetic phases I, II, and III. In panel (b), the arrows represent the spin direction and relative length. The spin structures for phases I and III can be determined directly from neutron diffraction Bragg intensities, while that for phase II is proposed based on the T and Q dependencies of inelastic magnetic scattering. More details are given in Sec. IV A 2.

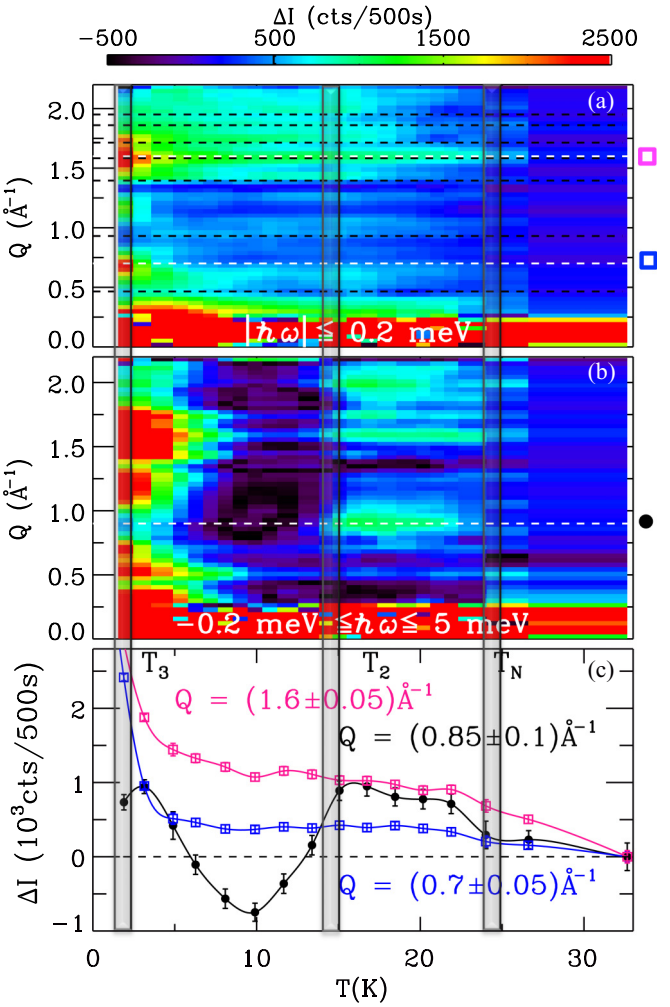

FIG. 3. Color image of (a) elastic and (b) energy-integrated neutron scattering versus temperature and wave vector. The data were acquired on the MACS instrument at NIST using the spectroscopic and energy-integrating detectors, respectively. Corresponding data sets acquired at $T = 32$ K were subtracted from each to expose small temperature-dependent effects. The incident neutron energy was 5 meV. Gray vertical regions indicate temperature intervals within 5% of the peak maxima in the magnetic specific heat [9]. Horizontal dashed black lines indicate the locations of allowed nuclear Bragg peaks. (c) Temperature dependence of the average scattering intensity in select ranges of wave vector transfer indicated by dashed white lines in (a) and (b). Black symbols are from the data presented in panel (b). Red and blue symbols are from (a). In all the figures where data are from neutron scattering experiments, the error bars indicate one standard deviation.

(vertical gray regions) are anomalies in the temperature-dependent neutron scattering data. Figure 3(c) provides a detailed view of the temperature-dependent intensity averaged over relevant ranges of wave vector transfer.

Below T_N we observe the development of Bragg diffraction for 1.5 $\text{Å}^{-1} < Q < 1.9$ Å^{-1} in Fig. 3(a). In being associated with a net increase in intensity, these features in the "thermo-diffractogram" are distinguished from the effects of thermal expansion, which produce matched minima and maxima surrounding each nuclear Bragg peak (horizontal dashed lines).

Figures 3(b) and 3(c) (black symbols and line) show a distinct reduction in inelastic scattering for temperatures below the characteristic temperature T_2 extracted from bulk properties. This observation was reproduced in experiments using both a flow cryostat and a dilution fridge, and the temperature and momentum regimes are inconsistent with contributions from cryogenic fluids such as nitrogen or helium. We associate this feature with a reduction in inelastic magnetic scattering for $T < T_2$ and $\hbar\omega < 5$ meV. The total scattering sum rule requires that reduced inelastic scattering appear elsewhere in $\mathcal{S}(Q\omega)$. One option is a shift of all the lost spectral weight beyond the 5 meV cutoff of the experiment [see Eq. (1)]. Alternatively a reduction in inelastic scattering can be associated with the development of elastic scattering and static correlations. In that case a possible explanation for the absence of elastic magnetic scattering associated with T_2 [see Fig. 3(a)] is that the associated component in $\mathcal{S}(Q\omega)$ is extinguished or severely weakened by the so-called polarization factor, which removes scattering associated with spin components parallel to wave vector transfer. This would be the case for a modulated in-plane spin structure in phase II where the staggered moment is oriented along the characteristic wave vector of the magnetic structure.

The clearest anomaly in scattering is associated with the lowest-temperature transition. The temperature regime for $T < T_3$ (phase III) is detailed in Fig. 4. Phase III is associated with the development of strong Bragg peaks and we shall argue that only in this phase is the spin direction perpendicular to the direction of modulation so the polarization factor does not extinguish the low-Q peaks. Figure 4(b) shows the integrated intensity, which develops in an order-parameter-like fashion for $T < T_3$, and Fig. 4(c) shows the half width at half maximum of the Lorentzian fit [inset to Fig. 4(c)]. After correcting for resolution effects the low-T limit corresponds to a correlation length above 75 Å.

While we have identified distinct anomalies in the T dependence of neutron scattering at each transition, all except perhaps those associated with T_3 are unusually broad in temperature compared to a standard second-order phase transition observed through diffraction with a cold neutron beam. This mirrors the specific-heat anomalies [9] and suggests we are dealing with crossover phenomena rather than critical phase transitions, which could result from disorder.

2. *Diffraction in each phase*

To elucidate the nature of each magnetic phase, we isolate the Q dependence of the associated scattering by subtracting

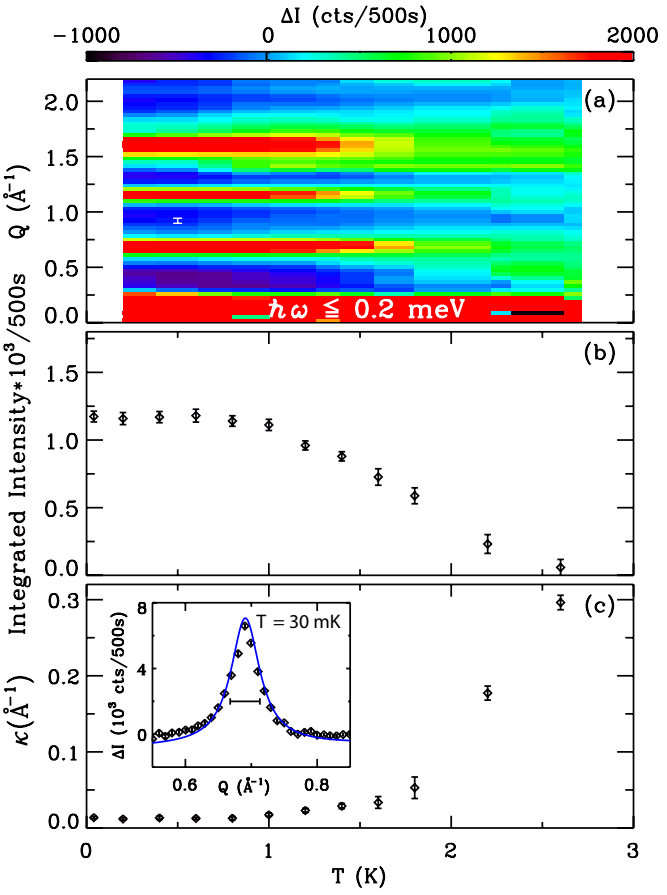

FIG. 4. (a) Image of elastic neutron scattering versus temperature and wave vector transfer in the low-temperature regime. Data collected at $T = 15$ K have been subtracted to remove scattering intensities of nuclear Bragg peaks. (b) Intensity and (c) inverse correlation length versus temperature extracted from fits of a Lorentzian convoluted with a Gaussian of the resolution width (horizontal bar within inset) to the most intense magnetic peak. Such a fit to the $T = 30$ mK data is shown in the inset to (c).

data collected for $T > T_N$ from high-statistics data acquired in each phase.

For phase I the difference pattern is shown in Fig. 5(a). Apart from the characteristic zigzag anomalies associated with thermal expansion (see Sec. II B), two distinct Bragg peaks are associated with phase I. A detailed view of these peaks is provided in Fig. 6. Discounting peak derivative line shapes indicated with the dashed lines described by Eq. (6), we identify two peaks at Å^{-1} and $Q = 1.63$ Å^{-1} (shadowed in bright green lines) whose intensities are less than 1% of nuclear peaks. Nearby there are no strong nuclear peaks so it is possible to obtain reliable magnetic diffraction. The region near $Q \sim 1.8$ Å^{-1} on the other hand is strongly influenced by strong nuclear Bragg peaks that do not subtract out well due to thermal expansion. The figure shows the peaks are resolution limited and this sets a low-temperature limit of 75 Å on the correlation length associated with translational symmetry breaking below T_N. The position of the peaks is indicated by the two vertical hatched regions in Fig. 7 for $Q > 1.5$ Å^{-1}. Assuming that a single propagation vector is associated with

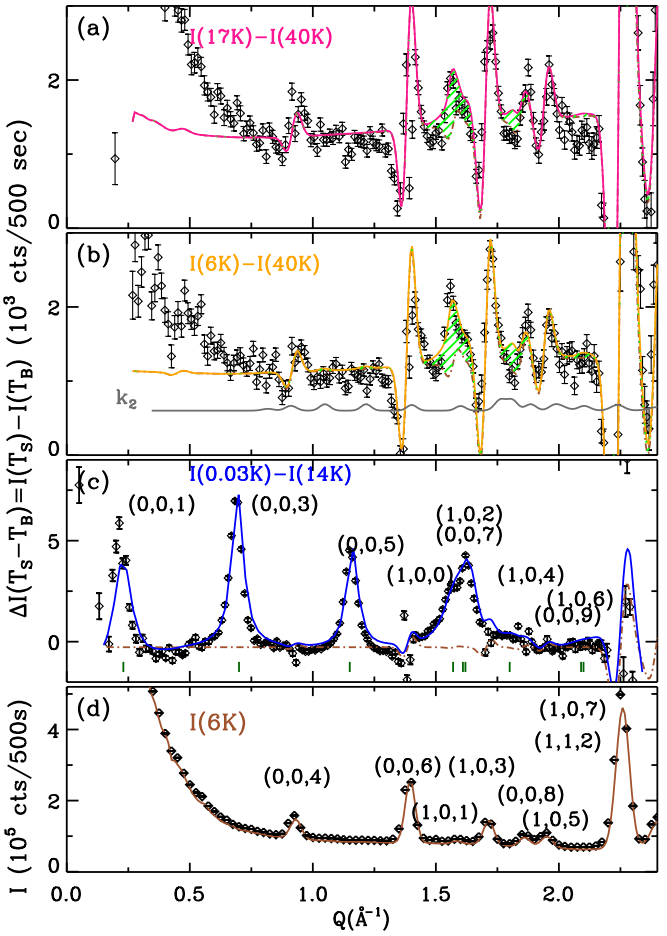

FIG. 5. Neutron diffraction patterns for $Ce_3Cu_4As_4O_2$ obtained at MACS with T = (a) 17 K, (b) 6 K, and (c) 30 mK. The fitted lines in (a)–(c) include a conventional Rietveld model for the magnetic scattering plus the peak derivative profile [dashed line in (c)] described in Sec. II B. The pattern in panel (b) includes the calculated diffraction pattern corresponding to the proposed spin structure in phase II (Fig. 2) with moment size listed in Table IV. It includes the contribution associated with wave vector $\mathbf{k}_1$ and $\mathbf{k}_2$. The calculated diffraction pattern from $\mathbf{k}_2$ with moment size 0.3 μ_B on Ce1 is also shown separately in solid gray line. The curve has been shifted downward by 500 counts. The line in (c) is a Rietveld fit to the structural peaks.

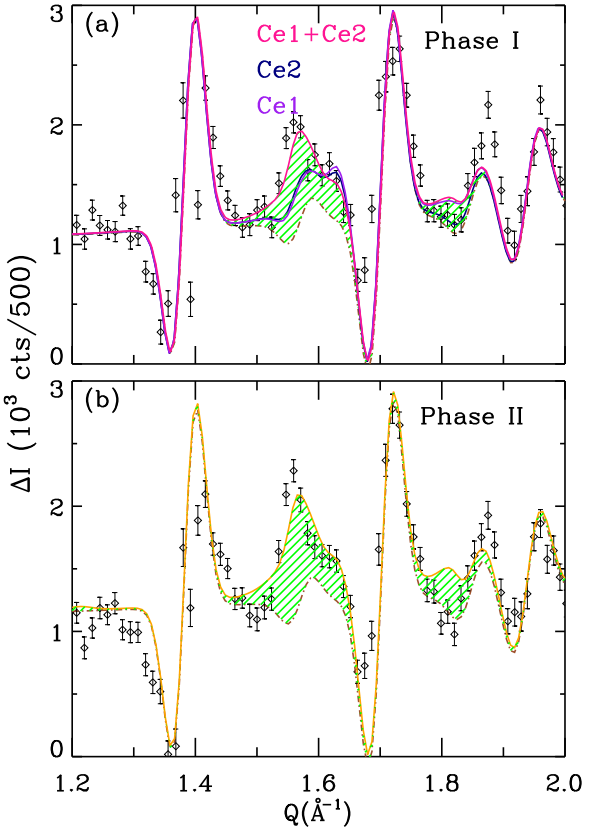

FIG. 6. Detailed Q dependence of neutron scattering data characterizing the magnetic order in (a) phase I (16 K $< T <$ 24 K) and (b) phase II (2 K $< T <$ 16 K). A background data set acquired at T = 40 K was subtracted to expose temperature-dependent features associated with the phase transitions. The lines through the data include the peak derivative features associated with thermal expansion [Eq. (6) and the calculated magnetic diffraction associated with the structures proposed in Fig. 2].

phase I, Fig. 7 shows this must be $\mathbf{k}_1 \equiv (0,0,1.0(2))$. The absence of magnetic Bragg peaks of the form $(0,0,2n+1)$, where n is an integer, indicates these peaks are extinguished by the polarization factor and so calls for spins polarization along **c**.

The diffraction pattern for phase II is shown in Fig. 5(b) with the detail in Fig. 6(b). Surprisingly there is virtually no change in the position or widths of magnetic Bragg scattering between phase I and phase II. The black symbols in Fig. 3(c), however, show that phase II is associated with the loss of inelastic scattering. As discussed above, the reduced inelastic scattering intensity in Fig. 4(b) for $T < T_2$ may result from shifting beyond the 5 meV cutoff, and/or static correlations and the associated Bragg diffraction may develop in phase II but be too weak for us to detect. Since the characteristic temperature T_2 is consistent with the second specific-heat anomaly [9], we shall associate the corresponding static spin structure that we propose in the analysis section with phase II. To better understand the dynamic correlations that are lost in phase II, Fig. 8 shows the Q dependence of the energy-integrated scattering in phase I, which is lost upon cooling into phase II. It takes the form of asymmetric peaks, which, in the direction of increasing Q, rise more abruptly than they decay. This Warren-like line shape [33] is a clear indication of low-dimensional correlations. We shall later show the correlations to be quasi-two-dimensional. In that case rods of scattering extend perpendicular to the plane of long-range correlations. The sharp leading edge is associated with these rods becoming tangents to the Ewald sphere and the long trailing tail results from the fraction of the Ewald sphere pierced by that rod decreasing in inverse proportion to the area of the sphere.

From Fig. 8 we see that the characteristic wave vector of the rod is 0.8 Å^{-1}. The proximity of this number to $a^*/2 = 0.77$ Å^{-1} indicates the spin fluctuations that vanish in phase II are associated with unit cell doubling in the basal plane. Possible explanations for the absence of a corresponding

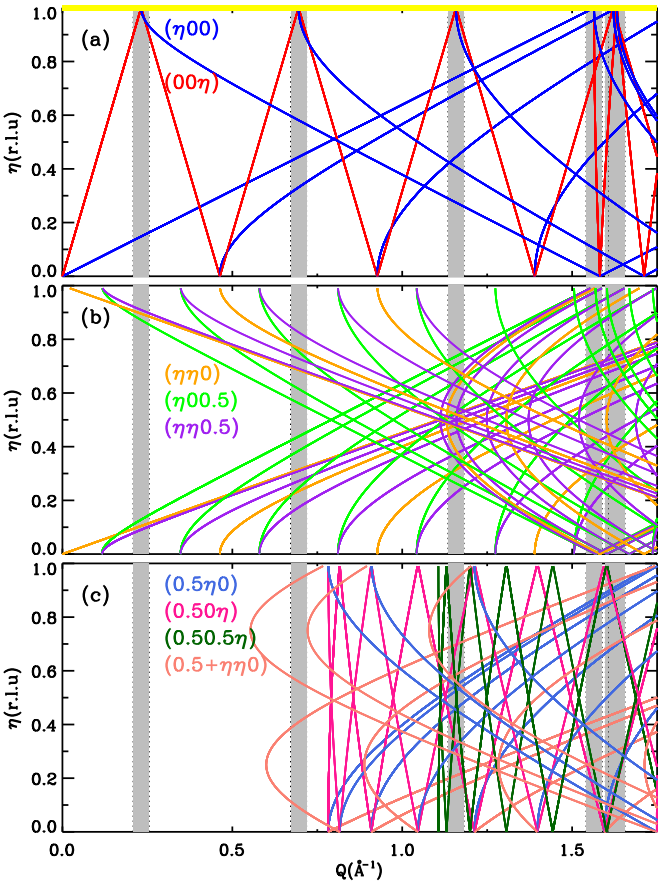

FIG. 7. Relationship between high-symmetry magnetic modulation wave vectors distinguished by colors and the location of magnetic satellite peaks in the powder diffraction pattern for $Ce_3Cu_4As_4O_2$. The vertical gray regions show the locations of the experimentally observed magnetic Bragg peaks. The low-T phase III has all indicated Bragg peaks whereas only the peaks near 1.5 Å^{-1} are visible in Fig. 6 for phases I and II. The calculated wave vector transfer associated with the horizontal yellow line in (a) $\mathbf{k}_1 = \mathbf{c}^*$ or equivalently $\mathbf{k}_1 = \mathbf{a}^*$ is consistent with the observed magnetic Bragg peaks. Panels (b) and (c) show the remaining singly indexed high-symmetry magnetic wave vectors that fail to account for the magnetic Bragg peaks observed in phase III.

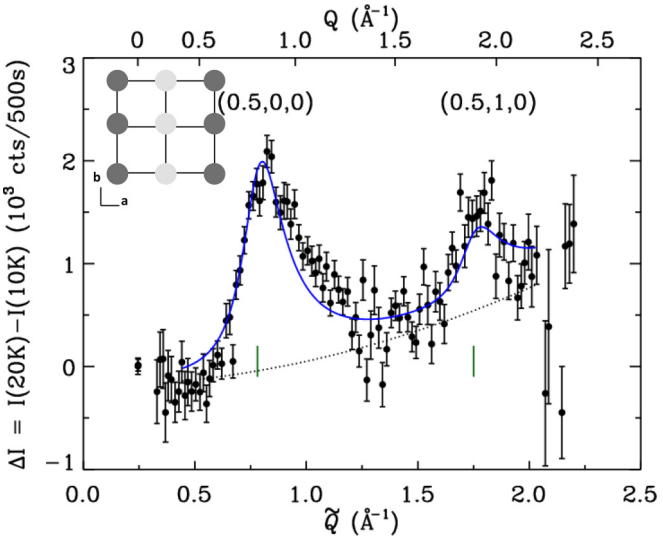

FIG. 8. $\tilde{Q}$-dependent intensity difference $\Delta I = I(20\,\mathrm{K}) - I(10\,\mathrm{K})$ from the energy-integrating detectors on the MACS spectrometer. The data are plotted as a function of wave vector transfer $\tilde{Q}(\theta,\omega)$ for energy transfer $\langle\hbar\omega\rangle = 1.2(3)$ meV inferred from the fitting analysis (see Sec. IV). The upper horizontal axis shows wave vector transfer for elastic scattering. The solid blue line is a Warren-like line shape for quasi-two-dimensional AFM correlations with characteristic wave vector $\mathbf{k}_2 = (1/2,0,0)$ and in-plane dynamic correlation length $\xi = 8.2(6)$ Å. The dashed line is a $\propto Q^2$ background ascribed to the difference in the Debye-Waller factor for incoherent scattering at the two temperatures involved. The inset shows the pattern of quasi-two-dimensional fluctuation associated with $\mathbf{k}_2$, with black and gray spots representing antiparallel spins. The proposed ordered state for phase II has spins parallel to $\mathbf{k}_2$ [Fig. 2(b)].

magnetic diffraction peak in Fig. 6(c) are (1) that a competing instability prevails so that static long-range AFM correlations of the $\mathbf{k}_2 = \mathbf{a}^*/2$ variety never materialize and (2) that a polarization factor extinguishes the magnetic Bragg peaks associated with this order in the low-Q regime where the present experiment has sufficient sensitivity to detect them.

As shown in Fig. 5(c), the strongest magnetic diffraction peaks are associated with phase III. Figure 7 shows that all peaks observed in phase III can be accounted for by a wave vector $\mathbf{k}_1 = \mathbf{c}^*$ or equivalently $\mathbf{k}_1 = \mathbf{a}^*$. The appearance of Bragg peaks of the form $(0,0,2n+1)$ in phase III implies there are spin components within the basal plane and a spin-flop transition between phases II and III. As shown in Sec. IV, the magnetic peaks are slightly broader than the nuclear peaks even at 30 mK indicating an element of disorder in the magnetic structure or strong thermal diffuse magnetic scattering with a length scale shorter than the coherence length of the chemical structure. Upon heating, the intensity of the magnetic peaks decreases precipitously above 2 K, though a broad feature remains at all magnetic Bragg positions up to $T = 2.6$ K. This indicates dynamic diffuse scattering near the critical temperature of the spin-flop transition.

C. Physical properties

1. Magnetization

The magnetization versus temperature was measured in different fields and the corresponding data are shown in Fig. 9(a). All magnetization measurements were conducted on polycrystalline samples, so the data represent the spherical average of the longitudinal response to the magnetic field $\mu_0 H$.

For temperatures below ~30 K, bifurcation between zero-field-cooled (ZFC) (solid lines) and field-cooled (FC) (dashed lines) magnetization data occurs for fields up to $\mu_0 H = 0.4$ T. To identify potential magnetic transitions, Fig. 9(b) shows $H^{-1}d(MT)/dT$, for which peaks are expected at magnetic Phase transitions [34]. Indeed, anomalies marked by vertical arrows occur near each of the transitions previously identified in specific-heat data [9]. As the field increases, $H^{-1}d(MT)/dT$ data [Fig. 9(b)] indicate that the lowest transition temperature T_3 increases and reaches ≈7 K for $\mu_0 H = 7$ T, while the upper two transitions at T_N and T_2 are largely unaffected by $\mu_0 H < 7$ T.

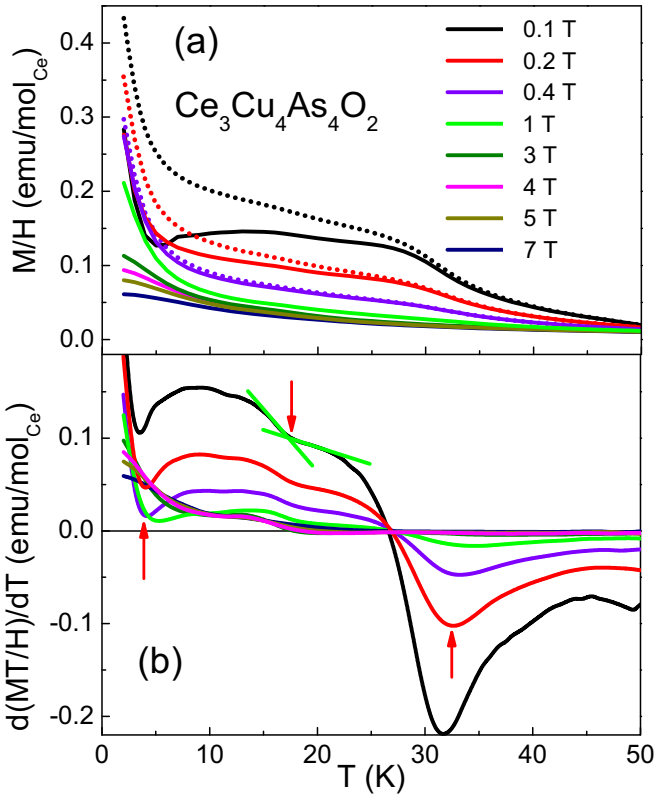

FIG. 9. (a) ZFC (solid lines) and FC (dotted lines) temperature-dependent M/H measured in applied magnetic fields up to $\mu_0 H = 7$ T. (b) The temperature derivatives of MH/T for different magnetic fields. The three transition temperatures previously inferred from specific-heat data [9] are marked by vertical arrows for $\mu_0 H = 0$. For SI units note the following conversion for the molar susceptibility: $\chi_M^{SI} = 4\pi \times 10^{-6} \chi_M^{cgs}$.

2. *Resistivity*

The field dependence of the resistivity measured on a dense polycrystalline sample is shown in Fig. 10. The resistivity increases upon cooling below room temperature, reaching a maximum at $T \approx 150$ K. The increase is typically associated with the single-ion Kondo effect, with the maximum signaling the onset of intersite coherence. Below 150 K, poor metallic behavior is observed, as the resistivity decreases with temperature, albeit with large residual resistivity values $\rho > 10$ mΩ cm. As the temperature decreases below 50 K, a difference between $\mu_0 H = 0$ (full symbols) and $\mu_0 H = 9$ T (open symbols) data develops, well above the upper transition temperature T_N inferred from specific-heat data [9]. Notably however, the magnetoresistance reaches a maximum near T_3, as shown below. The inset of Fig. 10 shows the low-temperature resistivity measured in different magnetic fields up to $\mu_0 H = 9$ T. The resistivity decreases monotonically with increasing magnetic field. For $\mu_0 H = 0$, a broad peak is observed near the anomalies in specific heat [9] and neutron diffraction, which shifts to higher temperature with increasing field. In phase III, Fermi liquid (FL) behavior is evidenced by the quadratic temperature dependence of the resistivity [Fig. 11(a)] up to $H \approx 3$ T. This behavior is reminiscent of a Kondo lattice system where the competition between

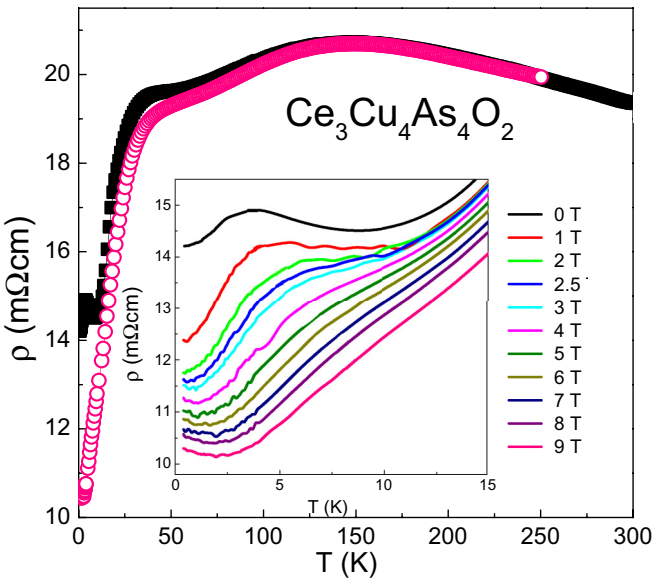

FIG. 10. The resistivity of $Ce_3Cu_4As_4O_2$ for $\mu_0 H = 0$ (squares) and $\mu_0 H = 9$ T (circles). Inset: Enlarged view of the low-temperature resistivity in this field range.

RKKY interections and Kondo screening gives rise to a peak around the coherence temperature T_{coh} and FL behavior below T_N [35]. For fields beyond $\mu_0 H \approx 2.5$–3 T however, a finite-T minimum in the resistivity develops, followed by a logarithmic increase of the resistivity for temperatures below $\approx$1 K as apparent in the semilog plot in Fig. 11(b). The $\rho \propto \log T$ behavior persists up to a temperature T^* that increases with magnetic field.

The origin of the logarithmic temperature dependence of resistivity in $Ce_3Cu_4As_4O_2$ is not clear: either the formation of a Kondo singlet [36] or weak Anderson localization in a 2D system [37] could lead to $\rho(T) \propto \log T$ behavior; however neither phenomenon is relevant for $Ce_3Cu_4As_4O_2$. For the former scenario, a magnetic field breaks up the Kondo singlet, which is inconsistent with the observation that the logarithmic temperature dependence extends over a larger-T regime for higher magnetic fields. In the latter scenario, the magnetic field may tune the localization-delocalization transition. The upturn in resistivity could be associated with weak localization [38]. However, localization should increase the resistivity beyond that of the delocalized state. Field-induced localization is thus not consistent with the observation of negative magnetoresistance in $Ce_3Cu_4As_4O_2$.

A complication in the interpretation of these data is that the polycrystalline nature of the sample implies the transport measurement is an average over all possible field and current directions with $\mathbf{H} \parallel \mathbf{J}$ in the tetragonal structure. For an anisotropic magnetic material such as $Ce_3Cu_4As_4O_2$ the high-field, low-T behavior could therefore be uncharacteristic and dominated by specific field directions.

The magnetoresistance is shown in Fig. 12 for $Ce_3Cu_4As_4O_2$ (symbols) and the nonmagnetic analog $La_3Cu_4As_4O_2$ (line). For the La compound, the magnetoresistance is positive and small (less than 5%), as expected for a normal metal where the Lorentz force introduces

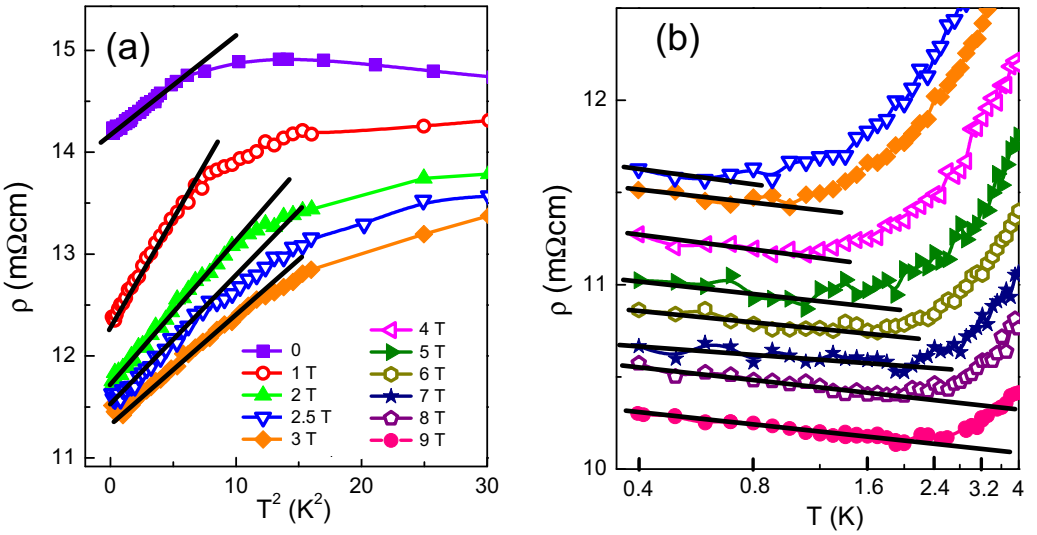

FIG. 11. (a) The quadratic dependence of resistivity for small magnetic fields between $\mu_0 H = 0$ T and $\mu_0 H = 3$ T. (b) The logarithmic dependence of resistivity for large fields between $\mu_0 H = 2.5$ T and $\mu_0 H = 9$ T.

electron scattering. For the Ce compound, the $T = 2$ K magnetoresistance is negative and reaches $\approx -30\%$ at $\mu_0 H = 9$ T. This suggests that the magnetism associated with the Ce^{3+} ions is responsible for the large magnetoresistance in $Ce_3Cu_4As_4O_2$.

The magnetoresistance for $Ce_3Cu_4As_4O_2$ is largest at $T = 2$ K, close to T_3. Similar large negative magnetoresistance was also observed in the Kondo lattice systems $Ce_2Ni_3Ge_5$, CeB_6, and $CeRhSn_2$ [39–41]. Above the magnetic ordering temperature, an important contribution to the resistivity is Kondo scattering of conduction electrons off local moments. By suppressing Kondo scattering the applied field may induce negative magnetoresistance. This negative magnetoresistance reaches a maximum at the magnetic ordering temperature where the magnetic fluctuations dominate all other contributions to the resistivity.

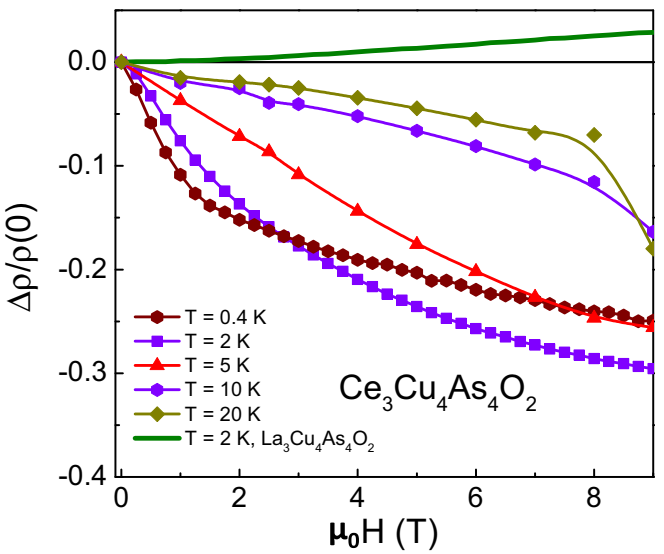

FIG. 12. Magnetoresistance data for $Ce_3Cu_4As_4O_2$ (symbols) for various temperatures, with the magnetoresistance of nonmagnetic $La_3Cu_4As_4O_2$ (line) at $T = 2$ K shown for comparison.

3. Specific heat

Additional information relevant to understanding the unusual low-T behaviors indicated by magnetization and transport measurements is provided by the field-dependent specific-heat data in Fig. 13. From Fig. 13(a), the broad

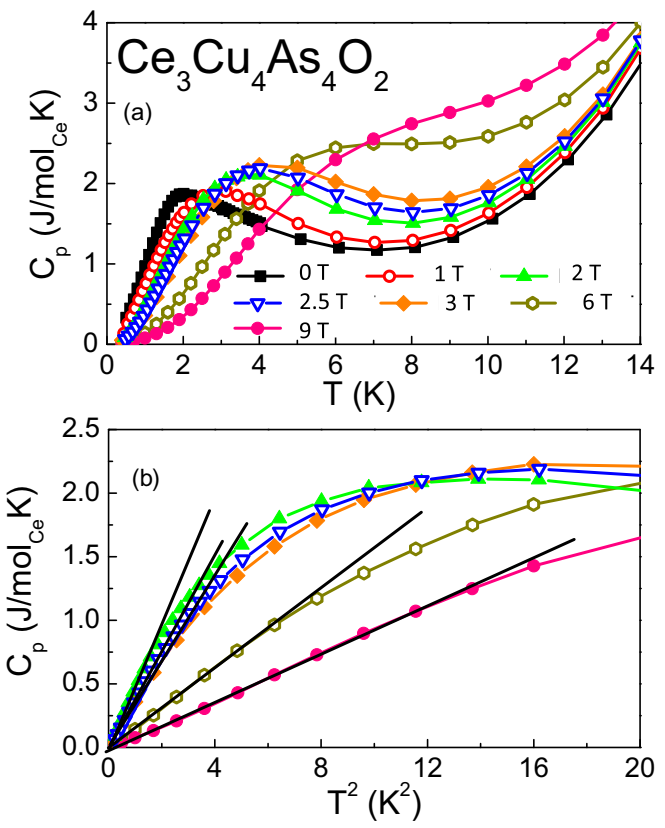

FIG. 13. (a) The specific heat of $Ce_3Cu_4As_4O_2$ measured from $T = 0.4$ K to $T = 14$ K, in applied magnetic fields between $\mu_0 H = 0$ and $\mu_0 H = 9$ T. (b) Quadratic temperature dependence of C_p in magnetic fields between $\mu_0 H = 2$ T and $\mu_0 H = 9$ T.

peak associated with low-T magnetic ordering at $T_3 = 2.0$ K shifts to higher temperatures and broadens for larger fields applied to the polycrystalline sample. C_p is quadratic in temperature for $\mu_0 H \geqslant 2.5$ T [Fig. 13(b)]. At $\mu_0 H = 9$ T, the quadratic dependence extends up to $T = 4$ K. This behavior can be associated with gapless excitations with a quasi-two-dimensional linear dispersion relation as in a two-dimensional antiferromagnet. In zero field the low-T state indicated in Fig. 2 would be expected to have an excitation gap similar in magnitude to T_3. The high-field $C_p(T) \propto T^2$ regime might be associated with specific field directions in the polycrystalline experiment that are transverse to the easy axes and induce gapless behavior.

IV. ANALYSIS

A. Magnetic structures

From the neutron scattering data presented in Sec. III B we have inferred the following principal features of magnetism in $Ce_3Cu_4As_4O_2$: For $T < T_N = 24$ K Ce spins are polarized along the tetragonal **c** axis, with a characteristic propagation vector $\mathbf{k}_1 = 001$. This structure persists in the second phase for $T < T_2 = 16$ K, which is marked by the *loss* of low-energy spin fluctuations that have quasi-two-dimensional spatial correlations, a characteristic wave vector $\mathbf{k}_2 = (0.5,0,0)$, and a component of polarization perpendicular to $\mathbf{k}_2$. Finally, for $T < T_3 = 2$ K there is a spin-flop transition where the orientation of spins modulated in accordance with $\mathbf{k}_1$ rotates from the **c** axis to the tetragonal basal plane.

While the the present powder diffraction data are insufficient to definitely determine the complex spin structures of $Ce_3Cu_4As_4O_2$, we shall develop a specific picture of the ordered spin structures that is consistent with the diffraction profiles and provides a logical sequence of phase transitions. One of the main outcomes that is supported by Rietveld analysis of the data is an association of the two wave vectors with the two different Ce sites in $Ce_3Cu_4As_4O_2$. The sequence of spin structures inferred from this analysis is shown in Fig. 2.

1. Phase I

We use representation theory to classify the magnetic structures with wave vector $\mathbf{k}_1 = (001)$ that can develop from the paramagnetic phase of space group $I4/mmm$ in a second-order phase transition. Using Kovalev notation [42], the representations associated with $\mathbf{k}_1$ and each of the two cerium sites decompose into irreducible representations (IRs) as follows. For the Ce1 cite associated with $CeRu_4As_4$ layers: $\Gamma_{\rm mag}(\text{Ce1}) = \Gamma_3 + 2\Gamma_9$. For the Ce2 sites associated with the Ce_2O_2 layers: $\Gamma_{\rm mag}(\text{Ce2}) = \Gamma_3 + \Gamma_2 + 2\Gamma_9 + 2\Gamma_{10}$.

There are a total of nine basis vectors [19] (BVs) and these are listed in Table III. For both cerium sites the two-dimensional Γ_9 and Γ_{10} IRs describe magnetic structures with in-plane moments while the one-dimensional Γ_3 and Γ_2 IRs describe structures with moments along the tetragonal c axis.

Because no magnetic peaks of the form $(0,0,2n+1)$ are observed for $T_2 < T < T_N$ (Fig. 5), the moment is oriented along the c axis and we must focus on the one-dimensional IRs Γ_2 and Γ_3. For the Ce1 sites this leaves just one option, namely Γ_3, which corresponds to the centered site antiparallel to the nearest neighbors (Fig. 2). For Ce2 sites there are two options corresponding to FM (Γ_2) or AFM (Γ_3) alignment of spins within a Ce_2O_2 bilayer.

TABLE III. The nine basis vectors associated with magnetic structures that transform according to irreducible representations of the $I4/mmm$ space group with propagation vector $\mathbf{k}_1 = (001)$. The irreducible representations and basis vectors were obtained using SARAh [19] and the notation is that of Kovalev [42].

IR	Atom	Basis Vectors		
		m_a	m_b	m_c
Γ_3	Ce_1	0	0	1
	Ce_2	0	0	1
Γ_9	Ce_1	1	0	0
		0	−1	0
	Ce_2	1	0	0
		0	−1	0
Γ_2	Ce_2	0	0	−1
Γ_{10}	Ce_2	−1	0	0
		0	1	0

Assuming the Γ_2 representation for Ce2 sites only (and no order on Ce1 sites) leads to $\chi^2 = 24$, which is larger than $\chi^2 = 18$ corresponding to Γ_3 with order on both cerium sites. Here the reduced χ^2 goodness is reported for difference data in the range $1.5\,\text{Å}^{-1} < Q < 1.8\,\text{Å}^{-1}$. Figure 6 shows three fit lines corresponding to Γ_3 order on Ce2, on Ce1 sites only and on both sites.The constrained differential line shape associated with thermal expansion is included with $\Delta a/a = 1.3\%$ and $\Delta c/c = 0.6\%$. The fit with order on both sites provides the best account for the relative intensity of the two peaks and the corresponding ordered moments inferred are $\mu_{\text{Ce}_1} = 0.14(6)\ \mu_B$ and $\mu_{\text{Ce}_2} = 0.18(2)\ \mu_B$. A sketch of the corresponding spin configuration is shown as phase I in Fig. 2(b). The weak nuclear Bragg peak (101) is close to the magnetic peaks. Subtle changes in the chemical structure could also play a role in the temperature dependence of diffraction in this Q range.

2. Phase II

While the present experiment detects no apparent elastic peaks upon entering phase II, a distinct *loss* of low-energy inelastic scattering is observed in the energy-integrating detectors of the MACS instrument for $T < T_2$ [Figs. 3(b) and 3(c)]. In Fig. 8 the broad anisotropic peaks associated with the scattering that vanishes for $T < T_2$ is compared to the spherical average of the following dynamic correlation function associated with quasi-two-dimensional magnetic correlations:

$$\mathcal{S}(\mathbf{Q}) = \sum_m \frac{\langle S^2\rangle \xi^2/\pi}{[1 + (\xi|\mathbf{Q}_\perp - \mathbf{Q_m}|)^2]^2}. \tag{9}$$

Here $\mathbf{Q}_m = \tau \pm \mathbf{k}_2$ indicates the location of critical points in the 2D reciprocal lattice. Because the incident neutron energy is similar to the energy scale of the spin system, actual wave vector transfer differs from that calculated neglecting energy

transfer as follows:

$$\tilde{Q}(\theta,\omega) = k_i \sqrt{2 - \frac{\hbar\omega}{E_i} - 2\sqrt{1 - \frac{\hbar\omega}{E_i}}\cos 2\theta}. \qquad (10)$$

With $\hbar\omega = 1.2(3)$ meV, in-plane correlation length $\xi = 8.2(6)$ Å, and an effective fluctuating moment of $(g_J\mu_B)^2\langle S^2\rangle \leqslant 0.3\mu_B^2$, this model provides a satisfactory account of the difference data in Fig. 8. Here we have plotted the data versus the inferred wave vector transfer for inelastic scattering $\tilde{Q}$ showing also wave vector transfer for elastic scattering on the upper horizontal axis.

In phase I, our analysis of the diffraction data indicates both Ce1 and Ce2 sites contribute to magnetic scattering associated with $\mathbf{k}_1$. But according to the analysis above, phase I also features strong inelastic scattering indexed by $\mathbf{k}_2 = (1/2,0,0)$. These dynamic correlations however fall out of view upon entering phase II [Fig. 3(c)]; we propose that T_2 is associated with the development of static order with $\mathbf{k}_2 = (1/2,0,0)$, since Ce2 sites play the dominant role in static order with $\mathbf{k}_1$ in phase I and probably also in phase III, while Ce1 sites appear to be almost irrelevant for $\mathbf{k}_1$ in phase III order. We propose that Ce1 sites drive the $\mathbf{k}_2$ correlations throughout. Specifically we pursue the hypothesis that the $\mathbf{k}_2 = (1/2,0,0)$ type scattering in Fig. 8 is associated with Ce1 sites. The total scattering can decrease if the kinematically accessible Bragg peaks of the corresponding order are extinguished by the polarization factor. Figure 5(b) includes the calculated elastic scattering that would result from the longitudinally polarized in-plane antiferromagnetic spin structure indicated in Fig. 2(b) for phase II with a moment size of 0.3 μ_B. Because spins are almost parallel to $\mathbf{k}_2$ at low wave vector transfer, this structure produces very little magnetic powder diffraction. The intensity is much weaker than the zigzag features from thermal expansion and the magnetic scattering due to $\mathbf{k}_1$ order. Hence, the development of $\mathbf{k}_2$ order with a moment size below 0.3 μ_B would go undetected in the present experiment. This structure is therefore a viable candidate to account for the loss of critical scattering with wave vector $\mathbf{k}_2$ without the appearance of appreciable magnetic Bragg scattering.

3. Phase III

The appearance of low-Q peaks in phase III of the $\mathbf{k}_1 = (001)$ variety is indicative of in-plane magnetic moments that are described by IR Γ_9 or Γ_{10} (Table III). Of these Γ_{10} is inconsistent with the observed relative intensities while Γ_9 provides the excellent fit shown in Fig. 5(c). The contribution to magnetic scattering from out-of-plane moments [Figs. 5(a) and 5(b)] is so weak that we cannot place meaningful limits on how much of this order remains in phase III. The experimental data in Fig. 5(c) are consistent with an AFM $\mathbf{k}_1 = (001)$ spin structure of the Γ_9 variety [Fig. 2(b)] with moments within the tetragonal basal plane. The total moment obtained is $(\mu_{Ce_1} + \mu_{Ce_2}) = 0.85(2)\ \mu_B$. Consistent with the assignment of Ce1 with moment $\leqslant 0.45\ \mu_B$ to the $\mathbf{k}_2$ structure, the Rietveld refinement displayed in Fig. 5(c) indicates the Ce1 site contributes less than 0.1 μ_B to the $\mathbf{k}_1$ structure in phase III.

In a field of 7 T the magnetization per cerium site reaches a value of 0.6 μ_B corresponding to 2/3 of the low-T ordered moment on the Ce2 sites, which make up 2/3 of the cerium in $Ce_3Cu_4As_4O_2$. This is consistent with the magnetization in 7 T of only the Ce2 sites that consist of FM layers leaving the Ce1 layers in the proposed in-plane $\mathbf{k}_2 = (0.5,0,0)$ type AFM structure. This hypothesis could be tested by higher field magnetization measurements.

B. Electronic structure

Density functional calculations were done on $Ce_3Cu_4As_4O_2$ for three types of magnetic configurations. The first is the ferromagnetic (FM) state. The second is the AFM $\mathbf{k}_1 = (001)$ structure, which corresponds to phase I in Fig. 2 and is referred to as AFM1. The third magnetic configuration examined is phase III of Fig. 2, with the same magnetic moment arrangements for Ce2 sites as in the AFM1 state and $\mathbf{k}_2 = (1/2,0,0)$ periodicity for Ce1 sites. This structure is referred to as AFM2. The magnetic unit cell for the AFM2 state is $2\times1\times1$ times the crystallographic unit cell.

Among all three magnetic configuration considered, AFM2 has the lowest energy. The relative energy for AFM2 state is $E(\text{AFM2}) - E(\text{FM}) = -127$ meV/f.u., while the relative energy for AFM1 is $E(\text{AFM1}) - E(\text{FM}) = 2$ meV/f.u. This comparison supports AFM2 as the ground state. For the AFM2 state, the DFT-inferred magnetic moments on both Ce sites are between $0.96 \sim 0.97\ \mu_B$, which is significantly larger than the experimentally observed values on Ce1 sites (0.45 μ_B), but close to the moment on Ce2 sites (0.85 μ_B). One possible reason for the reduced moment on Ce1 compared to DFT is that the Ce_1 atoms and As_2 atoms are both spatially and energetically close to each other, which might result in Kondo screening [25,43,44].

To examine the possibility of magnetism on the Cu site, a fixed spin moment calculation was performed for $La_3Cu_4As_4O_2$ (Fig. 14), the nonmagnetic analog of

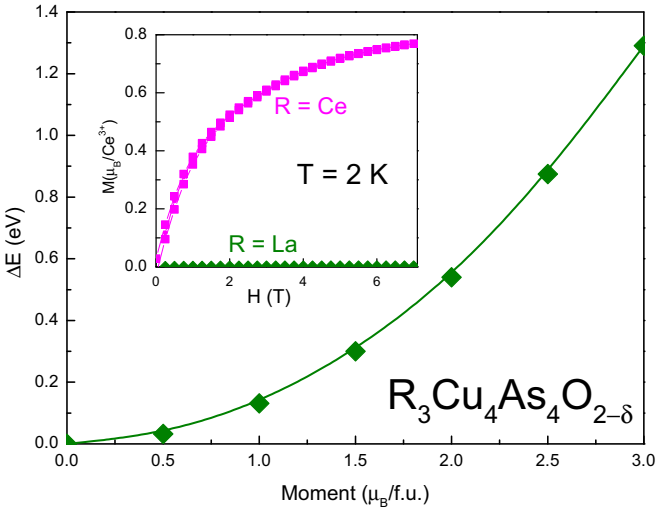

FIG. 14. Energy versus magnetic moment from the fixed spin moment calculation for $La_3Cu_4As_4O_2$, the nonmagnetic analog of $Ce_3Cu_4As_4O_2$. Inset: $M(H)$ isotherm for both $Ce_3Cu_4As_4O_2$ and $La_3Cu_4As_4O_2$.

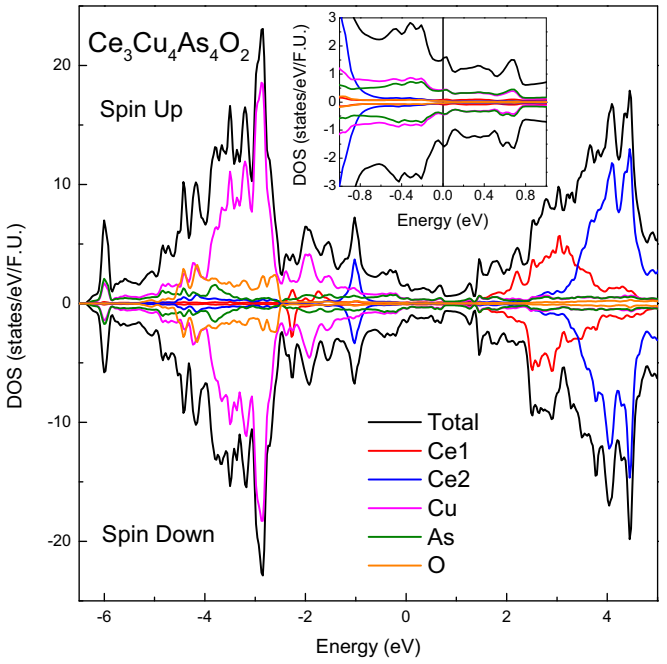

FIG. 15. The total and atom-projected DOS calculated for $Ce_3Cu_4As_4O_2$ in the AFM2 state. The spin-down DOS is multiplied by -1. Inset is an enlarged view near the Fermi level.

$Ce_3Cu_4As_4O_2$, with methods similar to those for the Ce compound. The energy of $La_3Cu_4As_4O_2$ increases monotonically with increasing spin moment, indicative of a paramagnetic ground state. This monotonic behavior implies there is no tendency for the 3*d* electrons to become magnetic, which is consistent with the experimental observations [9].

The density of states (DOS) for $Ce_3Cu_4As_4O_2$ in the AFM2 state is shown in Fig. 15. Unlike for Fe pnictides, the majority of the Cu bands lie close to the O bands, despite the fact that O has lower electronegativity than Cu. The increased energy of O bands might be due to their proximity to Ce atoms. At the Fermi level, Cu and As contribute most to the DOS. The nonzero DOS at the DFT Fermi level is indicative of a metal. The Ce_1 atoms have a lower energy, and their bands are broader than for the Ce_2 atoms.

The Cu 3*d* band is very broad, with a bandwidth of about 10 eV. Although centered around -3 eV, the tail of the 3*d* band is visible up to 5 eV, and the Fermi level just crosses this tail. This indicates a weakly correlated 3*d* band, consistent with a nonmagnetic state for Cu.

V. DISCUSSION

Having presented and analyzed comprehensive data for the magnetic and electronic properties of $Cu_3Cu_4As_4O_2$ we now discuss the overall physical picture of this material. Table IV provides a summary of the spin structures proposed for the three magnetic phases. While the upper two transitions mark the development of distinct magnetic modulations with wave vectors $\mathbf{k}_1 = (001)$ and $\mathbf{k}_2 = (1/2,0,0)$ in the Ce_2O_2 and the $CeCu_4As_4$ layers, respectively, the transition to phase III is a spin-flop transition where the staggered magnetization already established for Ce_2O_2 in phase I rotates into the basal plane. This last transition is by far the most prominent as observed by magnetic neutron scattering because it allows for diffraction at low Q which is extinguished by the polarization factor in the higher-temperature phases.

The lower transition to phase III might be understood as follows. If we allow for isotropic bilinear spin exchange interactions between different cerium sites then the effect of the Ce_2O_2 layers on the $CeCu_4As_4$ layers is analogous to a uniform magnetic field, which in phase II is oriented perpendicular to the staggered magnetization and along **c**. Rotation of the Ce_2O_2 magnetization into the basal plane can then be understood as the result of a competition between incompatible single-ion and/or exchange anisotropy for the Ce1 and Ce2 sites. Having ordered antiferromagnetically with spins within the basal plane in phase II, $CeCu_4As_4$ layers apparently have an easy-plane character. Phase I on the other hand demonstrates an easy-axis character to Ce_2O_2 layers. The final spin-flop transition at T_3 might then be understood as the easy-plane character prevailing as Ce_2O_2 spins rotate into the basal plane and perpendicular to $\mathbf{k}_2$. This is consistent with the diffraction data though these do not establish the orientation of Ce_2O_2 spins within the basal plane.

Comparison to $Pr_3Cu_4As_4O_{2-\delta}$ is instructive. The strength of RKKY exchange interactions can be expected to vary between rare-earth ions in accordance with the so-called de

TABLE IV. Overview of our working hypothesis for the magnetic structure in the three distinct phases of $Ce_3Cu_4As_4O_2$: phase I (16 K $< T <$ 24 K), phase II (2 K $< T <$ 16 K), and phase III ($T <$ 2 K). In the table, $\mathbf{k_1} = (0,0,1)$ and $\mathbf{k_2} = (1/2,0,0)$. The basis vector for one-dimensional IR Γ_2 associated with $\mathbf{k_2}$ is (100). The proposed structures are consistent with the experimental data but they are not uniquely determined by the experiment.

Site	Property	Phase III $T <$ 2 K		Phase II 2 K $< T <$ 16 K		Phase I 16 K $< T <$ 24 K
Ce1 in $CeCu_4As_4$	Propagation vector (**k**)	$\mathbf{k_1}$	$\mathbf{k_2}$	$\mathbf{k_1}$	$\mathbf{k_2}$	$\mathbf{k_1}$
	Classification (IR)	Γ_9	Γ_2	Γ_3	Γ_2	Γ_3
	Spin orientation	**b**	**a**	**c**	**a**	**c**
	Moment size (μ_B)	<0.1	$\leqslant 0.45$	0.17(2)	$\leqslant 0.3$	0.14(6)
Ce2 in Ce_2O_2	Propagation vector (**k**)	$\mathbf{k_1}$		$\mathbf{k_1}$		$\mathbf{k_1}$
	Classification (IR)	Γ_9		Γ_3		Γ_3
	Spin orientation	**b**		**c**		**c**
	Moment size (μ_B)	0.85(1)		0.22(3)		0.18(2)

Gennes factor $F = (g-1)^2 J(J+1)$, which is 0.18 for cerium and 0.8 for praseodymium for a ratio of $F(\mathrm{Pr})/F(\mathrm{Ce}) = 4.4$. While the ordered spin structures for $Pr_3Cu_4As_4O_{2-\delta}$ are as yet unknown, there are two phase transitions at $T_N = 35(3)$ K and $T_2 = 22$ K [9]. The enhancement of T_N is not nearly as large as might be expected based on de Gennes scaling but the similar ratio for T_2/T_N of approximately 1.5 for Ce and 1.6 for Pr is consistent with an analogy between phases I and II of the two compounds. The absence of a third transition for $Pr_3Cu_4As_4O_{2-\delta}$ is consistent with T_3 for $Ce_3Cu_4As_4O_2$ being contingent on competing anisotropies that might not exist for $Pr_3Cu_4As_4O_{2-\delta}$.

Replacing Ni for Cu in $CeNi_4As_4O_{2-\delta}$ results in just a single peak in the specific heat at $T_N = 1.7$ K [9]. The change in entropy up to 40 K, the effective moment, and the Weiss temperature are however similar to $CeCu_4As_4O_2$, which indicates the cerium moment persists. Increased magnetic frustration and quenched chemical or structural disorder are potentially relevant factors to account for the suppression relative to $Ce_3Cu_4As_4O_2$ of the higher-temperature transitions. Here we note that the rare-earth layers are separated by transition-metal ions so that all interlayer interactions must proceed through the copper or nickel layer. The dramatic effect of changing these layers from copper to nickel indicates the upper transitions are driven by interlayer interactions.

VI. CONCLUSION

In conclusion, field-dependent physical properties and neutron scattering measurements as well as band structure calculations were carried out on the layered transition-metal pnictide compound $Ce_3Cu_4As_4O_2$. The crystal structure resembles interleaving 122 and 1111 Fe pnictide structures, resulting in two rare-earth sites with very different local environments, and a complex interplay between their distinct magnetism. The neutron scattering measurements reveal three successive transitions, consistent with the magnetization and specific-heat measurements. For the first transition at $T_N = 24$ K, neutron scattering indicates alternating FM layers with spins oriented along c. Below the second transition $T_2 = 16$ K neutron scattering reveals the loss of spin fluctuations which we can account for by in-plane AFM ordering of the Ce1 site. The third transition $T_3 = 1.9$ K appears to be a spin-flop transition where all the magnetic moment directions switch to in-plane polarization. A large negative magnetoresistance ($\approx -30\%$) around T_3 is observed up to $\mu_0 H = 9$ T, which indicates a significant impact of magnetic fluctuations on transport behavior and for fields beyond 3 T, the temperature dependence of both resistivity and heat capacity deviate from that of a Fermi liquid. This is possibly due to the anisotropic quasi-two-dimensional nature of the electronic state as indicated by neutron data and the band structure calculations.

A curious feature of $Ce_3Cu_4As_4O_2$ is the broad nature of the specific-heat anomalies at T_N and T_2. The diffraction experiments presented here reveal magnetic order with a correlation length exceeding 75 Å but in harmony with the specific-heat data; the corresponding staggered magnetization emerges gradually upon cooling and without a critical onset (Figs. 3 and 4). The specific-heat and scattering data consistently point to crossover phenomena rather than actual phase transitions and thus the absence of true symmetry breaking. Potentially relevant features that could lead to this unusual situation are (1) disorder impacting the weak interactions between layers, (2) frustration, (3) the interplay of alternating layers of spins with distinct quasi-2D Ising transitions, and (4) Kondo screening. More detailed experiments on single-crystalline samples will be required to distinguish between these scenarios and achieve a deeper understanding of the unusual sequence of transitions in $Ce_3Cu_4As_4O_2$.

ACKNOWLEDGMENTS

Work at Rice University was supported by DOD PECASE. Work at IQM was supported by the US Department of Energy, Office of Basic Energy Sciences, Division of Material Sciences and Engineering, under Grant No. DE-FG02-08ER46544. This work utilized facilities supported in part by the National Science Foundation under Agreement No. DMR-1508249. The authors thank Andriy Nevidomskyy, Meigan Aronson, and Liang Zhao for useful discussions.

J.K.W. and S.W. contributed equally to the project.

[1] J. Kondo, Solid State Phys. **23**, 183 (1969).
[2] B. Coqblin and J. R. Schrieffer, Phys. Rev. **185**, 847 (1969).
[3] Z. Fisk, J. L. Sarrao, S. L. Cooper, P. Nyhus, G. S. Boebinger, A. Passner, and P. C. Canfield, Phys. B (Amsterdam, Neth.) **223-224**, 409 (1996).
[4] M. Dzero, K. Sun, V. Galitski, and P. Coleman, Phys. Rev. Lett. **104**, 106408 (2010).
[5] T. E. Mason, G. Aeppli, A. P. Ramirez, K. N. Clausen, C. Broholm, N. Stucheli, E. Bucher, and T. T. M. Palstra, Phys. Rev. Lett. **69**, 490 (1992).
[6] S. Doniach, Physica B & C **91**, 231 (1977).
[7] P. Coleman, C. Pepin, Q. M. Si, and R. Ramazashvili, J. Phys.: Condens. Matter **13**, R723 (2001).
[8] G. R. Stewart, Rev. Mod. Phys. **73**, 797 (2001).
[9] J. K. Wang, A. Marcinkova, C.-W. Chen, H. He, M. Aronson, and E. Morosan, Phys. Rev. B **89**, 094405 (2014).
[10] R. J. Cava, H. W. Zandbergen, J. J. Krajewski, T. Siegrist, H. Y. Hwang, and B. Batlogg, J. Solid State Chem. **129**, 250 (1997).
[11] J. W. Kaiser and W. Jeitschko, Z. Naturforsch. **57b**, 165 (2002).
[12] Y. Su, P. Link, A. Schneidewind, Th. Wolf, P. Adelmann, Y. Xiao, M. Meven, R. Mittal, M. Rotter, D. Johrendt, Th. Brueckel, and M. Loewenhaupt, Phys. Rev. B **79**, 064504 (2009).
[13] C. de la Cruz, Q. Huang, J. W. Lynn, J. Li, W. Ratcliff II, J. L. Zarestky, H. A. Mook, G. F. Chen, J. L. Luo, N. L. Wang, and P. Dai, Nature (London) **453**, 899 (2008).
[14] The identification of the commercial product does not indicate that it is endorsed by NIST or is recommended by NIST or that it is necessarily the best equipment for the purposes described.
[15] A. C. Larson and R. B. Von Dreele, General Structure Analysis System (GSAS), Los Alamos National Laboratory Report LAUR 86-748, 1994.

[16] J. A. Rodriguez, D. M. Adler, P. C. Brand, C. Broholm, J. C. Cook, C. Brocker, R. Hammond, Z. Huang, P. Hundertmark, J. W. Lynn, N. C. Maliszewskyj, J. Moyer, J. Orndorff, D. Pierce, T. D. Pike, G. Scharfstein, S. A. Smee, and R. Vilaseca, Meas. Sci. Technol. **19**, 034023 (2008).
[17] G. L. Squires, *Introduction to the Theory of Thermal Neutron Scattering* (Cambridge University Press, Cambridge, UK, 2012).
[18] H. M. Rietveld, J. Appl. Crystallogr. **2**, 65 (1969).
[19] J. A. S. Wills, Physica B **276–278**, 680 (2000).
[20] J. Rodriguez-Carvajal, Physica B **192**, 55 (1993).
[21] P. K. Blaha, K. Schwarz, G. Madsen, D. Kvasnicka, and J. Luitz, WIEN2k package, http://www.wien2k.at.
[22] J. P. Perdew, K. Burke, and M. Ernzerhof, Phys. Rev. Lett. **77**, 3865 (1996).
[23] D. A. Andersson, S. I. Simak, B. Johansson, I. A. Abrikosov, and N. V. Skorodumova, Phys. Rev. B **75**, 035109 (2007).
[24] H. M. Alyahyaei and R. A. Jishi, Phys. Rev. B **79**, 064516 (2009).
[25] S. Kawarazaki, M. Sato, Y. Miyako, N. Chigusa, K. Watanabe, N. Metoki, Y. Koike, and M. Nishi, Phys. Rev. B **61**, 4167 (2000).
[26] O. Stockert, E. Faulhaber, G. Zwicknagl, N. Stusser, H. S. Jeevan, M. Deppe, R. Borth, R. Küchler, M. Loewenhaupt, C. Geibel, and F. Steglich, Phys. Rev. Lett. **92**, 136401 (2004).
[27] L. P. Regnault, W. A. C. Erkelens, J. Rossat-Mignod, P. Lejay, and J. Flouquet, Phys. Rev. B **38**, 4481 (1988).
[28] N. H. van Dijk, B. Fåk, T. Charvolin, P. Lejay, and J. M. Mignot, Phys. Rev. B **61**, 8922 (2000).
[29] C. Broholm, J. K. Kjems, W. J. L. Buyers, P. Matthews, T. T. M. Palstra, A. A. Menovsky, and J. A. Mydosh, Phys. Rev. Lett. **58**, 1467 (1987).
[30] J. Zhao, Q. Huang, C. de la Cruz, S. Li, J. W. Lynn, Y. Chen, M. A. Green, G. F. Chen, G. Li, Z. Li, J. L. Luo, N. L. Wang, and P. Dai, Nat. Mater. **7**, 953 (2008).
[31] Y. Luo, H. Han, H. Tan, X. Lin, Y. Li, S. Jiang, C. Feng, J. Dai, G. Cao, Z. Xu, and S. Li, J. Phys.: Condens. Matter **23**, 175701 (2011).
[32] S. Wu, W. A. Phelan, L. Liu, J. C. Neuefeind, M. Feygenson, M. B. Stone, J. Morey, D. Tam, S. Dunsiger, Y. J. Uemura, T. M. McQueen, C. L. Broholm, and others, Incommensurate magnetism near quantum criticality in the Kondo lattice CeNiAsO (unpublished).
[33] B. E. Warren, Phys. Rev. **59**, 693 (1941).
[34] M. E. Fisher, Philos. Mag. **7**, 1731 (1962).
[35] H. Schweitzer and G. Czycholl, Phys. Rev. Lett. **67**, 3724 (1991).
[36] A. C. Hewson, *The Kondo Problem to Heavy Fermions* (Cambridge University Press, Cambridge, UK, 1997), Vol. 2.
[37] P. W. Anderson, Phys. Rev. **109**, 1492 (1958).
[38] N. Giordano, W. Gilson, and D. E. Prober, Phys. Rev. Lett. **43**, 725 (1979).
[39] Z. Hossain, S. Hamashima, K. Umeo, T. Takabatake, C. Geibel, and F. Steglich, Phys. Rev. B **62**, 8950 (2000).
[40] N. Ali and S. B. Woods, J. Appl. Phys. **57**, 3182 (1985).
[41] Z. Hossain, L. C. Gupta, and C. Geibel, J. Phys.: Condens. Matter **14**, 9687 (2002).
[42] O. V. Kovalev, *Representations of the Crystallographic Space Groups: Irreducible Representations, Induced Representations, and Corepresentations*, 2nd ed., edited by H. T. Stokes and D. M. Hatch (Gordon and Breach, London, 1993).
[43] Wei Bao, P. G. Pagliuso, J. L. Sarrao, J. D. Thompson, Z. Fisk, J. W. Lynn, and R. W. Erwin, Phys. Rev. B **62**, R14621(R) (2000).
[44] D. J. Singh and M.-H. Du, Phys. Rev. Lett. **100**, 237003 (2008).